

# New insights into the structural transition from $\text{UO}_{2+x}$ to $\text{U}_3\text{O}_7$ by Quantitative Raman spectroscopy

Received 00th January 20xx,  
Accepted 00th January 20xx

DOI: 10.1039/x0xx00000x

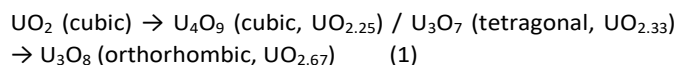
Jone M. Elorrieta,<sup>a</sup> Abel Milena-Pérez,<sup>\*a</sup> Jean-François Vigier<sup>b</sup>, Laura J. Bonales<sup>a</sup> and Nieves Rodríguez-Villagra<sup>a</sup>

The study of uranium oxides at different conditions is of paramount importance in the nuclear field, especially regarding characterization of the spent nuclear fuel behavior in dry storage scenarios. This paper reports results of a XRD and Raman analysis on four powdered samples prepared in order to cover a specific stoichiometry range in  $\text{UO}_{2+x}$ , *i.e.*  $x=0.24, 0.26, 0.28$  and  $0.30$ . XRD results reveal a clear increase of the average tetragonal distortion with the increase in oxidation degree, with the main phase detected for all the samples being a weakly tetragonal phase identified as  $\text{U}_3\text{O}_{7-z}$  ( $c/a << 1.032$ ).  $\text{U}_4\text{O}_9$  has not been detected in any sample. The Raman study carried out consists of both a qualitative and a quantitative analysis. The former, where a profile analysis has been performed on the acquired spectra, shows that the most intense bands (centered at  $\sim 455$  and  $\sim 635 \text{ cm}^{-1}$ ) are actually a doublet each, in agreement with a previous experimental study. Moreover, this work shows, for the first time, that the band at  $\sim 160 \text{ cm}^{-1}$  is also a doublet, which makes its classical assignment no longer obvious. The most important and original results from this study are obtained by applying Quantitative Raman Spectroscopy (QRS). This analysis shows that the second contribution at  $\sim 475 \text{ cm}^{-1}$  to the known  $\text{T}_{2g}$  mode increases its relative intensity with the oxidation degree. This contribution may be related to the tetragonal distortion occurring in the cubic  $\text{UO}_2$  lattice due to the addition of interstitial oxygen, based on its comparison with the obtained XRD outcomes. In addition, the so-called "defects band" (centered at around  $600 \text{ cm}^{-1}$ ) presents a remarkable kink, of around  $20 \text{ cm}^{-1}$ , in its Raman shift between  $\text{UO}_{2.26}$  and  $\text{UO}_{2.28}$ . Such behavior might be directly associated with the observed appearance of the stoichiometric  $\text{U}_3\text{O}_7$  phase ( $c/a=1.032$ ) for  $\text{UO}_{2.28}$  and  $\text{UO}_{2.30}$ .

## 1. Introduction

$\text{UO}_2$ , as the standard matrix of the widely used Light Water Reactors (LWR) nuclear fuels, is irradiated in nuclear power plants, which leads to microstructural changes, mainly as a result of the fission products formation and the subsequent production of oxygen stoichiometry defects.

The interaction of uranium and oxygen is complex to analyze as there are numerous stable stoichiometric phases with various polymorphs for a certain O/U ratio, the presence of sub- and super-stoichiometric domains, and the potential interconversion between phases depending on the conditions, *e.g.* temperature, gaseous environment and moisture.<sup>1, 2</sup> Oxidation of the fuel matrix,  $\text{UO}_2$ , is assumed to proceed by first forming either  $\text{U}_4\text{O}_9$  or  $\text{U}_3\text{O}_7$ , phases that are denser than the initial  $\text{UO}_2$  as a consequence of a net contraction.<sup>3</sup> Further oxidation to  $\text{U}_3\text{O}_8$  implies a density decrease of about 23%<sup>4</sup> and 36%  $\Delta V/V_0$  swelling compared to original  $\text{UO}_2$ .<sup>5</sup> The generally accepted reaction of  $\text{UO}_2$  to form  $\text{U}_3\text{O}_8$  follows a two-step process with intermediate phases, as described in Equation 1:



The first step in the  $\text{UO}_2$  oxidation reaction has been extensively investigated, although some transitions are not yet fully understood. At least three compounds are typically involved:  $\text{UO}_2$ ,  $\text{U}_4\text{O}_9$  and  $\text{U}_3\text{O}_7$ , which at the same time can also display a wide variety of non-stoichiometry regions.<sup>6, 7</sup> First of

all, when oxidation starts, the cubic fluorite structure of  $\text{UO}_2$  accommodates extra oxygen. This gives rise to a variety of phases generally denoted as  $\text{UO}_{2+x}$ , where  $x$  indicates the excess of oxygen incorporated into the cubic lattice (it must be noted that the hereinafter mentioned hyper-stoichiometric  $\text{UO}_{2+x}$  refers to a compound whose O/U value is interpreted as a global/average value). The fluorite type structure is maintained up to the  $\text{U}_4\text{O}_9$  structure,<sup>8, 9</sup> as the excess oxygen atoms are ordered in a super-lattice of cubooctahedral-type clusters.<sup>10, 11</sup> Further oxidation implies a gradual distortion of crystal structure, derived from the transition from fluorite-type cubic to tetragonal symmetry. This indicates the formation of the  $\text{U}_3\text{O}_7$  phase or, as reported by some studies, of the less tetragonally-distorted  $\text{U}_3\text{O}_{7-z}$  phase (with a much lower axial ratio,  $c/a << 1.032$ ).<sup>11-14</sup> Allen *et al.*<sup>15</sup> describe both the structures of  $\text{U}_4\text{O}_9$  and  $\text{U}_3\text{O}_7$  as higher fluorite-based structures of  $\text{UO}_2$  with periodic arrangements of oxygen defect clusters. At this point, the orthorhombic oxidation product  $\text{U}_3\text{O}_8$  is formed at the expense of  $\text{U}_3\text{O}_7$ .<sup>3, 6, 7, 9, 16, 17</sup>

The determination of the non-stoichiometric uranium oxide phases (the O/U ratio) is typically observed by means of thermogravimetric and X-Ray Diffraction (XRD) methods, especially by the latter because it determines the phases and it allows validating the thermogravimetric results obtained. Knowing the hyper-stoichiometric composition of uranium oxides is essential for assessing the behavior of the spent fuel matrix at medium-long term storage. In particular, Raman spectroscopy can be effectively used to trace characteristic spectra of materials and to derive the oxidation phases of uranium, as we have recently demonstrated.<sup>18, 19</sup> Furthermore, it is a non-destructive chemical analysis technique, samples need no particular preparation, it is versatile (*e.g.* it can be applied to solids, liquids and gases) and allows "remote" and portable characterization, minimizing the exposure to

<sup>a</sup> Centro de Investigaciones Energéticas, Medioambientales y Tecnológicas (CIEMAT). Avda. Complutense 40, 28040, Madrid (Spain).

<sup>b</sup> European Commission, Joint Research Centre (JRC). 76125, Karlsruhe (Germany).

hazardous samples. Owing to these features, Raman spectroscopy is a suitable technique for the analysis of radioactive materials.<sup>20-23</sup> However, one of the main drawbacks of this technique is the limited reference libraries available for researchers to identify uranium oxide compounds (Table 1), especially for the measurement of intermediate oxides. As a matter of fact, the number of studies reporting the identification of  $U_4O_9$  and  $U_3O_7$  is scarce, and it is not clear to which of the two phases the Raman features should be assigned.

Table 1 Some representative references with reported values of the observed Raman bands in uranium oxides.

Compound	Raman shift /cm <sup>-1</sup>	Raman active mode	Reference
$UO_2$	445-450	$T_{2g}$	<sup>24-26</sup>
	1150	2LO	<sup>27</sup>
$U_4O_9$	160		<sup>28-30</sup>
	465	$T_{2g}$	<sup>30</sup>
	627-630		<sup>27, 28, 31</sup>
	877		<sup>31</sup>
$U_3O_7$	155		<sup>32</sup>
	465-475	$T_{2g}$	<sup>32</sup>
	630		<sup>29</sup>
	230-241		<sup>25, 30</sup>
$U_3O_8$	336-351	$A_{1g}$	<sup>20, 25</sup>
	405-412	$A_{1g}$	<sup>20, 25</sup>
	474-493	$A_{1g}$ or $E_g$	<sup>20, 25</sup>
	638-640	overtones of U-O stretching $A_{1g}$ and $E_g$	<sup>25</sup>
	738-753	$A_{2u}$	<sup>20, 25, 33, 34</sup>
	798-811	overtones of U-O stretching $A_{1g}$ and $E_g$	<sup>20, 25</sup>

The  $UO_2$  fluorite structure (Fm-3m symmetry group) is well characterized by one first-order Raman mode, corresponding to the  $T_{2g}$  mode of symmetric stretching U-O at  $\sim 445\text{ cm}^{-1}$ , and a second-order mode, the 2 ( $T_{1u}$ LO) at  $\sim 1150\text{ cm}^{-1}$ , which is the first overtone of the LO.<sup>24-27</sup> Raman spectrum of  $U_3O_8$  usually reveals a strong multiplet between 300 and  $550\text{ cm}^{-1}$ ,<sup>33-39</sup> but a precise analysis is still needed due to the high number of Raman active modes in the structure.<sup>36</sup> Various experimental and theoretical studies have attempted to characterize intermediate uranium oxides.<sup>20, 27-32, 40-43</sup> Unfortunately, Raman analysis of the intermediate phase  $U_3O_7$  is scarcely supported by the literature,<sup>44</sup> due to its similarity to  $U_4O_{9+y}$ ,<sup>10</sup> when disorder associated with oxygen cluster defects appears. In order to ensure an unambiguous identification of unknown products found on altered nuclear fuel samples, a spectral

database needs to be set up and compiled from synthetic and natural standard materials.<sup>26</sup>

To add further demonstration of Raman spectroscopy as a suitable technique in the nuclear field, it is applied in this study to  $UO_{2+x}$  powdered samples ( $0.24 < x < 0.30$ ) with the goal of using it as a both qualitative and quantitative tool (the so-called Quantitative Raman Spectroscopy, QRS). Our recent results obtained by Raman spectroscopy will be presented, discussed and compared to the results obtained applying the Rietveld refinement method (XRD characterization) to the same samples, in order to provide a useful chemical identification tool with an extended reference library. These new data set recorded at different O/U ratios will help to improve the analysis of the  $UO_2$  matrix degradation behavior and, in particular, to gain new insights into its structural transition towards the tetragonal  $U_3O_7$  phase.

## 2. Experimental

### 2.1. Sample preparation

Four  $UO_{2+x}$  powder specimens with a range in stoichiometry between  $x=0.24$  and  $x=0.30$  were prepared by subjecting near-stoichiometric  $UO_2$  powder to  $300^\circ\text{C}$  in a  $N_2/O_2$  mixture during different intervals of time. The starting  $UO_2$  powder was obtained by first oxidizing crushed and sieved in-house manufactured  $UO_2$  pellets up to  $U_3O_8$  and subsequently reducing the resulting powder. The particle size of the attained near-stoichiometric  $UO_2$  was around  $15\text{ }\mu\text{m}$ . This methodology has been optimized and applied in our laboratory previously, details are given elsewhere.<sup>18</sup>

### 2.2. Characterization techniques

Thermogravimetric analyses (TGA) for the purpose of determining the stoichiometry of the prepared samples were performed with a TA Instruments Q50 thermobalance. The method consisted in oxidizing the samples to  $U_3O_8$  by heating them up to  $700^\circ\text{C}$ , with a heating rate of  $10^\circ\text{C}$  per minute, under a constant synthetic air flow (60 mL/min). The average stoichiometry or O/U ratio of the initial specimens was then estimated by assuming full conversion to  $U_3O_8$ , the latter having been confirmed by X-ray diffraction.

Raman spectra were acquired by means of a Horiba LabRAM HR Evolution spectrometer, at an excitation wavelength of 632.8 nm provided by a He-Ne laser. The laser beam was focused onto the sample through the 50x objective of an Olympus BX41 microscope. The scattered radiation was then collected in backscattering geometry, dispersed using a 600 grooves/mm holographic grating and recorded using a CCD detector (256 x 1024 pixels), obtaining a  $\sim 1\text{ cm}^{-1}/\text{pixel}$  spatial resolution and a spectral resolution of better than  $2\text{ cm}^{-1}$ . For the analysis of each oxide, around 20 spectra were recorded at different locations of the sample, which were summed afterwards. A typical spectrum was obtained over the wavenumber range  $70$ - $1280\text{ cm}^{-1}$ , optimizing in all cases both the excitation power and acquisition times in order to prevent further oxidation due to the laser.<sup>45</sup> The acquired spectra were recalibrated with the emission lines of a Ne lamp.

Room temperature X-ray diffraction (XRD) measurements on the prepared oxides were carried out by a Bruker D8 Advance Eco diffractometer, using Cu K $\alpha$  radiation ( $\lambda = 1.54056 \text{ \AA}$ ) and operating at 40 kV and 25 mA. Bragg-Brentano configuration geometry was applied. The  $2\theta$  range covered was from  $20^\circ$  to  $130^\circ$ , with a scanning step size of  $0.04^\circ$ . Structural analyses were performed by the Rietveld method using JANA2006 software.<sup>46</sup> The various systematic sources of error were minimized by both a correct alignment of the instrument and the measurement of a certified  $\text{Al}_2\text{O}_3$  pattern.

### 3. Results

#### 3.1. Oxidation degree characterization

As previously mentioned, four  $\text{UO}_{2+x}$  powdered samples with different oxidation degree ( $\text{UO}_{2.24}$ ,  $\text{UO}_{2.26}$ ,  $\text{UO}_{2.28}$  and  $\text{UO}_{2.30}$ , with a relative sampling error around 1%) were prepared in a thermobalance by applying a thermal treatment. Afterwards, the stoichiometry of the samples was confirmed by oxidizing an aliquot of each sample up to  $\text{U}_3\text{O}_8$ , and determining through the mass gain the initial "x" in the formula  $\text{UO}_{2+x}$ . It should be underlined that the deduced average O/U is expressed as  $\text{UO}_{2+x}$  for simplicity but this does not necessarily implies a single-phase compound. Fig. 1 shows the weight change curves of the final oxidation of the samples.

As can be seen in Fig. 1, the sequence of the samples follows the calculated stoichiometry. All the displayed curves show the typical two-step oxidation process of unirradiated  $\text{UO}_2$  ( $\text{UO}_2 \rightarrow \text{U}_4\text{O}_9/\text{U}_3\text{O}_7 \rightarrow \text{U}_3\text{O}_8$ ).<sup>3, 47, 48</sup> Given that a higher initial hyper-stoichiometry of the samples makes the first step of the reaction to be shorter, the latter curves entail a qualitative confirmation of the intended sequential stoichiometry of the prepared oxides. The precise mass gain calculation, carried out assuming the final product to be  $\text{U}_3\text{O}_8$ , corroborates this fact.

#### 3.2. XRD analysis

In addition to TGA, the oxidation of the different samples has been evaluated by powder XRD analyses. The obtained diffractograms have been analyzed in detail and interpreted in terms of the aforementioned  $\text{UO}_2$  oxidation process. In this way, Rietveld refinement<sup>49</sup> has been performed to estimate the proportion of the different phases present in the samples and their lattice parameters. The refinement yields very successful results when considering the presence of  $\text{UO}_2$  and/or  $\text{U}_3\text{O}_7$  phases (see Fig. 2). All the structural parameters have been fixed according to the following well-established structures: the  $\text{UO}_2$  compound was refined in the  $Fm-3m$  space group and  $\text{U}_3\text{O}_7$  in the  $P4_2/nmm$  space group with atomic positions fixed according to the ones described by Leinders *et al.*<sup>13, 50</sup> Even if the full  $\text{U}_3\text{O}_7$  structure is better described in the bigger lattice with  $P4_2/n$  space group, the use of the  $P4_2/nmm$  lattice gives an average view of the cuboctahedral oxygen positions and is justified by two main reasons: (1) the detailed  $P4_2/n$  structure only generates a large number of the substructural diffraction peaks which are too weak to be visible with powder XRD technique and are irrelevant for the refinement, and (2) the use of the averaged  $P4_2/nmm$  lattice provides a much more straightforward comparison between

the fluorite mother structure and its tetragonal distortion into  $\text{U}_3\text{O}_7$  after oxidation.

The refined parameters are presented in Table 2. In addition, the axial ratio ( $c/a$ ) of each detected phase has been calculated and included in **Error! No se encuentra el origen de la referencia.**, as well as the estimated average axial ratio of each sample ( $(c/a)_{av}$ ).

Table 2 Refined parameters of  $\text{UO}_2$  ( $Fm-3m$ ),  $\text{U}_3\text{O}_{7-z}$  ( $P4_2/nmm$ ) and  $\text{U}_3\text{O}_7$  ( $P4_2/nmm$ ) phases in the  $\text{UO}_{2+x}$  studied samples, and characteristic parameters of the stoichiometric  $\text{U}_3\text{O}_7$  phase for reference.

Samp le	Phase	a (Å)	b (Å)	c (Å)	c/a	(c/a) <sub>av</sub>	[Phas e] %
$\text{UO}_{2.24}$	$\text{U}_3\text{O}_{7-z}$	5.41 7(1)	5.417(1)	5.480(1)	1.01 2	1.01	91(1)
	$\text{UO}_2$	5.46 5(1)	5.465(1)	5.465(1)	1		9(1)
$\text{UO}_{2.26}$	$\text{U}_3\text{O}_{7-z}$	5.41 3(1)	5.413(1)	5.480(1)	1.01 2	1.01 2	1
	$\text{U}_3\text{O}_{7-z}$	5.40 4(1)	5.404(1)	5.493(1)	1.01 7	1.02	79(1)
$\text{UO}_{2.28}$	$\text{U}_3\text{O}_7$	5.38 0(1)	5.380(1)	5.550(1)	1.03 2	0	21(1)
	$\text{U}_3\text{O}_{7-z}$	5.40 4(1)	5.404(1)	5.493(1)	1.01 6	1.02	75(1)
$\text{UO}_{2.30}$	$\text{U}_3\text{O}_7$	5.37 9(1)	5.379(1)	5.550(1)	1.03 2	0	25(1)
	$\text{U}_3\text{O}_7$	5.37 8	5.378	5.550	1.03 2	-	-
$\text{U}_3\text{O}_7$ ref. <sup>13</sup>	$\text{U}_3\text{O}_7$						

For  $\text{UO}_{2.24}$  sample, about 9% of remaining  $\text{UO}_2$  phase is detected with a lattice parameter slightly below the expected value of  $5.471 \text{ \AA}$ .<sup>50</sup> This deviation is probably due to a minor hyper-stoichiometry of the oxide, with an estimated value of  $\text{UO}_{2.02}$  according to one of our previous studies.<sup>18</sup> For clarity, we will continue to refer to this phase as  $\text{UO}_2$ . The main phase is well refined using the  $\text{U}_3\text{O}_7$  model, but the lattice parameters obtained show only a weak tetragonal distortion, with axial ratio ( $c/a$ ) strongly below the expected value of 1.032.<sup>51</sup> This weak tetragonal distortion is in agreement with previous observations and it is explained by the substoichiometry of the  $\text{U}_3\text{O}_{7-z}$  oxide.<sup>52-54</sup> This  $\text{U}_3\text{O}_{7-z}$  phase is the main phase of all four samples. For  $\text{UO}_{2.26}$  sample, only  $\text{U}_3\text{O}_{7-z}$  phase is observed, with similar lattice parameters to the ones of  $\text{UO}_{2.24}$ . For  $\text{UO}_{2.28}$  and  $\text{UO}_{2.30}$  samples, instead, the  $\text{U}_3\text{O}_{7-z}$  phase shows a slight increase of the tetragonal distortion (*i.e.* an increase of the  $c/a$  ratio), suggesting an increase of the oxygen content in the oxide. In addition, a second tetragonal phase with a  $c/a$  ratio of 1.032 is observed in these two samples, in agreement with stoichiometric  $\text{U}_3\text{O}_7$ .<sup>54</sup> In particular,  $\text{UO}_{2.26}$  presents a moderately lower fraction of the latter  $\text{U}_3\text{O}_7$  phase (21%) than that detected for  $\text{UO}_{2.28}$  (25%).

These XRD results can be used as a corroboration of the increase in oxidation degree of the studied samples.

### 3.3. Raman analysis

Fig. 3 presents the acquired Raman spectra of the four studied  $\text{UO}_{2+x}$  oxides, with a stoichiometry ranging from  $x=0.24$  to  $x=0.30$ , as well as the typical spectrum of non-stoichiometric  $\text{UO}_2$  for reference purposes. As a matter of fact, the Raman spectra of the  $\text{UO}_{2+x}$  samples should derive from the original  $\text{UO}_2$  spectrum, as a consequence of its related structure. The Raman spectrum of  $\text{UO}_2$  has been described in detail in the literature,<sup>18, 28, 29, 41</sup> its main Raman features being the  $\text{T}_{2g}$  mode at  $\sim 445 \text{ cm}^{-1}$  (U-O bond stretching), the LO phonon band at  $\sim 570 \text{ cm}^{-1}$  and its first overtone (2LO) at  $\sim 1140 \text{ cm}^{-1}$ , as can be well appreciated in Fig. 3. In contrast, at first glance, the spectra corresponding to the prepared  $\text{UO}_{2+x}$  oxides contain at least four broad bands centered at around 160, 270, 455 and 635  $\text{cm}^{-1}$ . When comparing these spectra with the one characteristic of non-stoichiometric  $\text{UO}_2$ , the typical extensive distortion of the cubic fluorite lattice due to the redistribution of excess oxygens into cuboctahedral clusters<sup>18, 20, 28, 29</sup> can be clearly deduced from the behavior of the main Raman bands (see Fig. 3): 1) the shift of the  $\text{T}_{2g}$  mode from around 445  $\text{cm}^{-1}$  up to around 455  $\text{cm}^{-1}$  in the oxidized samples, 2) the absence of the 2LO phonon band, 3) the great intensity of the  $\sim 635 \text{ cm}^{-1}$  feature, widely ascribed to a high concentration of such clusters, and 4) the appearance of a contribution at around 160  $\text{cm}^{-1}$ .

With the aim of also corroborating by means of Raman spectroscopy the progressive increase in oxidation degree in our samples, we have assessed the shift in wavenumber suffered by the oxygen-clusters-related  $\sim 635 \text{ cm}^{-1}$  band. In this way, by applying the second derivative method<sup>55</sup> on all the acquired spectra, the central position of this main band has been obtained for each sample. These positions or Raman shifts are shown in Fig. 4 as a function of the increase in oxidation degree (or  $x$  in  $\text{UO}_{2+x}$ ).

As can be seen in Fig. 4, the increase in the oxidation degree of the samples is reflected in the shifting to higher wavenumbers of the 635  $\text{cm}^{-1}$  band, where an approximately linear trend is found, going from 630  $\text{cm}^{-1}$  in  $\text{UO}_{2.24}$  up to around 642  $\text{cm}^{-1}$  in  $\text{UO}_{2.30}$ . Given that this band is commonly related to oxygen cuboctahedral clusters,<sup>18, 20</sup> the observed Raman shift as a function of  $x$  might be due to the increasing amount of these clusters and their subsequent continuous approach, resulting in shorter distances between the involved oxygen atoms.<sup>56</sup>

A deeper discussion on the evolution of the other observed Raman bands will be addressed in the next section.

## 4. Discussion

The first step of the oxidation of uranium dioxide is an extensively studied process in which, nevertheless, some transitions still remain unclear or not fully understood. In principle, it is commonly accepted that at least three phases are involved in such transformation:  $\text{UO}_2$ ,  $\text{U}_4\text{O}_9$  and  $\text{U}_3\text{O}_7$ . First of all, the cubic fluorite structure of  $\text{UO}_2$  gives place to a number of well-known reflections.<sup>50</sup> When oxidation starts, extra oxygen being accommodated in the lattice gives as a result the shift of the XRD pattern to higher  $2\theta$  values.<sup>29</sup> This slightly oxidized structure is generally denoted as  $\text{UO}_{2+x}$ , in

which “ $x$ ” is dependent on the pattern shifting and it is quantifiable.<sup>18</sup> At a later stage of oxidation, the organization of interstitial oxygen atoms in a cuboctahedral configuration within the fluorite mother structure gives rise to the  $\text{U}_4\text{O}_9$  phase, which is also a fluorite-related structure.<sup>8, 9</sup> If oxidation continues, such a cubic distribution is no longer stable and a tetragonal distortion starts to take place, eventually leading to the full formation of  $\text{U}_3\text{O}_7$ .<sup>12, 13</sup> At this point, the effect on the XRD pattern is the appearance of a splitting of the mother fluorite diffraction lines.

As can be seen in Fig. 2a, the diffractogram obtained for  $\text{UO}_{2.24}$  shows the mentioned splitting of the  $\text{UO}_2$  phase peaks. The same line-splitting is observed for the other samples (Fig. 2b-d). This proves that our four  $\text{UO}_{2+x}$  oxides present a tetragonally-distorted structure, *i.e.* contain a high fraction of a  $\text{U}_3\text{O}_7$ -related phase as detected in the Rietveld refinement. The extent of such overall distortion can be assessed taking into consideration the average axial ratio of each sample ( $(c/a)_{av}$ ), which clearly reveals a larger tetragonal distortion of the lattice when stoichiometric  $\text{U}_3\text{O}_7$  is present (see Table 2).

A remarkable outcome of our XRD analysis is that  $\text{U}_4\text{O}_9$  has not been detected for any sample, even if its presence at a very low concentration cannot be fully excluded as it would partially overlap with the  $\text{U}_3\text{O}_{7-z}$  phase. From a phenomenological point of view, these results can be justified with the mechanism of oxidation itself. The first two reaction steps ( $\text{UO}_2 \rightarrow \text{U}_4\text{O}_9$  and  $\text{U}_4\text{O}_9 \rightarrow \text{U}_3\text{O}_7$ ) are controlled by diffusion of oxygen,<sup>54</sup> which increasingly distorts the lattice. In unirradiated  $\text{UO}_2$ , as is our case, this distortion usually takes place in a faster way, making the dominant phase which reaches a certain level of oxidation to be  $\text{U}_3\text{O}_7$ , and thus leading to an unlikely detection of  $\text{U}_4\text{O}_9$ . On the contrary, the presence of transuranic elements and fission products formed in the spent nuclear fuel during irradiation promotes the stabilization of the cubic  $\text{U}_4\text{O}_9$  phase.<sup>57-60</sup> Some published works have also proved that, in unirradiated  $\text{UO}_2$ , the fast formation of the  $\text{U}_3\text{O}_7$  phase is due to the appearance of a thin oxidation layer on the  $\text{UO}_2$  substrate, that eventually cracks and exposes fresh  $\text{UO}_2$  to the oxidizing agent.<sup>61, 62</sup>

Taking as a basis this discussion on the XRD results, the obtained Raman spectra have been used to thoroughly study the structural changes occurring in these  $\text{UO}_{2+x}$  oxides with the increase in oxidation degree. For this purpose, a profile analysis of the spectra has been performed, taking into account the individual contributions previously identified via the second derivative method. As an example, Fig. 5 shows the spectrum and the second derivative of the Raman features obtained in the analysis of the  $\text{UO}_{2.28}$  sample, in which the different contributions to each Raman band can be easily visualized.

In so doing, several overlapping bands have been revealed in the four Raman spectra. These analyses are shown in Fig. 6 (a-d) and have been obtained by fitting the peaks to Pseudo-Voigt functions. As can be seen, the same seven bands have been detected for every spectrum, located at around 150, 175, 260, 455, 475, 600 and 635  $\text{cm}^{-1}$ . This means that the previously noticed four broad bands (160, 260, 455 and 635

$\text{cm}^{-1}$ ) comprise in fact seven individual bands, with three of the four initial features being actually a doublet each. If one compares the obtained bands with those generally observed in the Raman spectra of  $\text{UO}_{2+x}$  oxides,<sup>18, 20, 28, 29</sup> the most remarkable feature appears to be the contribution at around  $475 \text{ cm}^{-1}$ , which is not evident at all at first sight. Only He and Shoesmith<sup>29</sup> reported the presence of a band at  $\sim 470 \text{ cm}^{-1}$  that they associated with the presence of the tetragonal  $\text{U}_3\text{O}_7$  phase, and assigned it to the  $E_g$  (U-O) stretching Raman mode that also appears in the spectrum of  $\text{U}_3\text{O}_8$ . Thus, the appearance of such a band in all our spectra suggests that  $\text{U}_3\text{O}_7$  (or at least a tetragonal distortion of the lattice) is present, to a greater or lesser extent, in the four studied oxides. In order to assess the tetragonal distortion of the  $\text{UO}_2$  cubic structure caused by the increasing concentration of oxygen, we have applied the QRS method to calculate the ratios of integrated intensities of the  $475$  and  $455 \text{ cm}^{-1}$  ( $T_{2g}$ ) bands ( $I_{475}/I_{455}$ ). As can be seen in Fig. 7, the ratio  $I_{475}/I_{455}$  increases continuously from  $\text{UO}_{2.24}$  to  $\text{UO}_{2.28}$ , *i.e.* as the oxidation degree increases, and then seems to remain quite steady (within the overlapping error range) between  $\text{UO}_{2.28}$  and  $\text{UO}_{2.30}$ . This evidences that, the higher the excess oxygen concentration, the larger the amount of tetragonal distortion domains arising in the  $\text{UO}_{2+x}$  lattice, until at some point above  $\text{UO}_{2.26}$  these domains are present to such a large extent that a global tetragonal distortion of the lattice is noticed. The latter would thus lead us to consider the possibility that for both  $\text{UO}_{2.28}$  and  $\text{UO}_{2.30}$  a significant transformation to the tetragonal  $\text{U}_3\text{O}_7$  phase has taken place. This outcome is actually in very good agreement with the previously described XRD results. In particular, one can observe that the  $I_{475}/I_{455}$  ratio of the  $\text{UO}_{2+x}$  samples presents a similar behavior with  $x$  to that of the average axial ratio ( $(c/a)_{av}$  in Table 2): it increases up to  $\text{UO}_{2.28}$  and then it seems to stabilize for  $\text{UO}_{2.30}$ . This suggests that the  $475 \text{ cm}^{-1}$  band might be strongly related to the  $c$  axis of the tetragonally-distorted lattice.

On the other hand, several studies have ascribed the existence of a band at  $\sim 160 \text{ cm}^{-1}$  to a significant distortion of the cubic  $\text{UO}_2$  lattice,<sup>28, 29</sup> yet with slightly different interpretations: in some cases considering this peak a fingerprint of the  $\text{U}_4\text{O}_9$  phase,<sup>28</sup> whereas in other cases perceiving it as the confirmation of  $\text{U}_3\text{O}_7$  formation in  $\text{UO}_{2+x}$  oxides.<sup>29</sup> As already mentioned, we have also observed a broad contribution at around  $160 \text{ cm}^{-1}$  in the four acquired  $\text{UO}_{2+x}$  spectra (see Fig. 3), which corroborates the assumption of the presence of some structural change in all our samples. The detection of the previously described band at around  $475 \text{ cm}^{-1}$  and its assignment might prove the tetragonal distortion of the lattice. Anyhow, the profile analysis of the  $160 \text{ cm}^{-1}$  band shows that this contribution is constituted by two bands, located at  $\sim 150$  and  $\sim 175 \text{ cm}^{-1}$  respectively (Fig. 6). In fact, if one looks carefully at the  $\text{U}_4\text{O}_9$  Raman spectrum acquired by Desgranges *et al.* with the  $457 \text{ nm}$  laser,<sup>28</sup> an overlapping doublet centered at around  $160 \text{ cm}^{-1}$  is clearly discernible. Therefore, we conclude that the so far commonly quoted  $\sim 160 \text{ cm}^{-1}$  band corresponds, indeed, to a doublet of peaks. Although He and Shoesmith<sup>29</sup> assigned their band at  $\sim 155 \text{ cm}^{-1}$  to the  $B_{1g}$  mode (by comparison with the optical modes

contained in experimental spectra of the tetragonal phase of  $\text{ZrO}_2$ ), the present observation of a doublet makes the assignment of the two corresponding peaks no longer obvious. Given the poor signal-to-noise ratio obtained for  $\text{UO}_{2.24}$  and  $\text{UO}_{2.30}$  in that low-wavenumber region of the spectra, we have not been able to properly evaluate the behavior of the  $\sim 150$  and  $\sim 175 \text{ cm}^{-1}$  bands as a function of the oxidation degree, what might help in the understanding of their origin. Regarding the analysis of the only feature that is not composed by two individual contributions, the broad band at  $\sim 260 \text{ cm}^{-1}$  has been generally assigned in the literature to the doubly degenerate  $F_{1u}$  IR active TO mode, which is initially Raman-forbidden in the cubic  $\text{UO}_2$  structure but becomes allowed once this original structure is distorted.<sup>28, 29, 63, 64</sup> As for the band centered at around  $600 \text{ cm}^{-1}$ , usually referred to as the “defects band” in non-stoichiometric  $\text{UO}_{2+x}$  oxides,<sup>18, 20, 29, 41, 42</sup> we have detected an intriguing feature with regard to its behavior as  $x$  (in  $\text{UO}_{2+x}$ ) increases from  $0.24$  to  $0.30$ . In fact, we have analyzed the Raman shift (or position) evolution of this band and noticed that, while in  $\text{UO}_{2.24}$  and  $\text{UO}_{2.26}$  it is found at the  $\sim 590$  to  $600 \text{ cm}^{-1}$  range, it appears at a much higher Raman shift ( $\sim 615 \text{ cm}^{-1}$ ) in both  $\text{UO}_{2.28}$  and  $\text{UO}_{2.30}$ , as can be seen in Fig. 8. Such a remarkable shift in position, of approximately  $20 \text{ cm}^{-1}$ , must be directly associated with the appearance of the stoichiometric  $\text{U}_3\text{O}_7$  phase for  $\text{UO}_{2.28}$  and  $\text{UO}_{2.30}$  as observed by XRD. In fact, a comparable kink can be appreciated for the average axial ratio ( $(c/a)_{av}$  in Table 2) between  $\text{UO}_{2.26}$  and  $\text{UO}_{2.28}$  samples. This is due to the much larger  $c/a$  ratio of stoichiometric  $\text{U}_3\text{O}_7$  compared to the one of  $\text{U}_3\text{O}_{7-z}$ , what induces the transition from a weak to a significant tetragonal distortion of the lattice beyond  $\text{UO}_{2.28}$ .

## 5. Conclusions

A detailed analysis of phase transitions in  $\text{UO}_{2+x}$  oxides has been carried out, covering the range  $0.24 < x < 0.30$ . The appropriate increase in the oxidation degree of the prepared samples has been confirmed by the weight gain curves obtained by thermogravimetric analysis, which has also been used to precisely determine the average stoichiometry of such oxides.

By means of the XRD technique, the Rietveld refinement method has been used in order to determine the composition of uranium oxides phases present in the samples. The results indicate that  $\text{U}_3\text{O}_{7-z}$ , a phase with a weaker tetragonal distortion ( $c/a < 1.032$ ) than stoichiometric  $\text{U}_3\text{O}_7$ , is the main phase detected for all four samples. For  $\text{UO}_{2.24}$ , this phase is observed together with a slightly hyperstoichiometric  $\text{UO}_2$  phase. For  $\text{UO}_{2.26}$ , it is the only phase identified. And for  $\text{UO}_{2.28}$  and  $\text{UO}_{2.30}$  samples, it is detected together with the stoichiometric  $\text{U}_3\text{O}_7$  phase. As a matter of fact,  $\text{U}_4\text{O}_9$  has not been identified in our XRD analysis. The latter conclusion is justified by comparison of the obtained lattice parameters with data from the literature, lying in good agreement with other studies reporting the presence of  $\text{U}_3\text{O}_7$  in the studied O/U ratio range.

Regarding Raman spectroscopy results, and at first glance, the detection of four Raman features, and in particular the upshift

of the broad band centered at around  $635\text{ cm}^{-1}$  in the oxidized samples (from  $\text{UO}_{2.24}$  to  $\text{UO}_{2.30}$ ), confirms the increase in oxidation degree, by comparison with the Raman bands obtained and described for the  $\text{UO}_2$  spectrum. However, the profile analysis carried out on the four Raman spectra has revealed that some of these Raman bands actually correspond to a doublet each, providing new insights on the structural changes occurring in the current  $\text{UO}_{2+x}$  range. This qualitative analysis has confirmed the presence of two contributions to the  $\sim 455$  and  $\sim 635\text{ cm}^{-1}$  modes. In addition, and as a novelty, it has revealed that the band located at  $\sim 160\text{ cm}^{-1}$ , previously ascribed to a distortion of the  $\text{UO}_2$  lattice, is found to be a doublet (centered at around 150 and  $175\text{ cm}^{-1}$ ), which highlights the necessity of re-evaluating the assignment of this band to the  $\text{B}_{1g}$  mode.

On the other hand, Quantitative Raman Spectroscopy (QRS) has been applied to the acquired spectra of all samples, using the qualitative findings of doublets at the different bands and the results obtained by XRD as a basis for the conclusions obtained. These outcomes have been interpreted as follows:

- a) A contribution related to  $\text{U}_3\text{O}_7$  has been found at around  $475\text{ cm}^{-1}$ , overlapping with the known  $\text{T}_{2g}$  mode ( $\sim 455\text{ cm}^{-1}$  for  $\text{UO}_{2+x}$  oxides). The ratio of integrated intensities of both bands ( $I_{475}/I_{455}$ ) has been analyzed, finding that this value grows steadily from  $\text{UO}_{2.24}$  to  $\text{UO}_{2.28}$ , reaching a statistically similar value in  $\text{UO}_{2.28}$  and  $\text{UO}_{2.30}$ . This behavior confirms the increasing presence of a tetragonal distortion of the  $\text{UO}_2$  lattice with higher oxygen content, and is in agreement with the XRD results. Indeed, given the clear similarities between the behavior of the  $475\text{ cm}^{-1}$  band and that of the average  $c/a$  ratio we postulate that this band might be strongly related to the  $c$  axis of the tetragonally-distorted lattice.
- b) An intriguing behavior has been noticed for the so-called "defects band" in  $\text{UO}_2$ , *i.e.* the band centered at about  $600\text{ cm}^{-1}$ . In fact, the analysis of the Raman shift of this feature leads to the finding that, while in  $\text{UO}_{2.24}$  and  $\text{UO}_{2.26}$  it is detected at the  $\sim 590$  to  $600\text{ cm}^{-1}$  range, it appears at a much higher Raman shift ( $\sim 615\text{ cm}^{-1}$ ) in both  $\text{UO}_{2.28}$  and  $\text{UO}_{2.30}$ . This remarkable position shift might be associated with the appearance of the stoichiometric  $\text{U}_3\text{O}_7$  phase for these two samples, which causes the transition from a weak to a significant tetragonal distortion of the structure.

This work improves our understanding of non-stoichiometric uranium oxides, which can be used as a basis for researchers focused on the alteration of spent fuel matrix under interim or final disposal conditions, including nuclear forensic laboratories.

## Conflicts of interest

There are no conflicts to declare.

## Notes and references

1. M. A. Burton, A. W. Auner, J. C. Crowhurst, P. S. Boone, L. A. Finney, D. G. Weisz, B. Koroglu, I. Jovanovic, H. B. Radousky and K. B. Knight, *Scientific reports*, 2022, **12**, 4030.
2. H. Idriss, *Surface Science Reports*, 2010, **65**, 67-109.
3. R. J. McEachern and P. Taylor, *Journal of Nuclear Materials*, 1998, **254**, 87-121.
4. B. O. Loopstra, *Acta Crystallographica*, 1964 **17**, 651 -654.
5. G. Rousseau, L. Desgranges, G. Rousseaux, J. C. Niepce, G. Rousseau, G. Baldinozzi and J. F. Berar, *Journal de Physique 4*, 2004, 127-134.
6. G. Leinders, T. Cardinaels, K. Binnemans and M. Verwerft, *Inorganic Chemistry*, 2018, **57**, 4196-4204.
7. G. Leinders, O. Ozdemir, J. Pakarinen, R. Delville and M. Verwerft, Prague, Czech Republic, 2018.
8. L. Desgranges, G. Baldinozzi, D. Siméone and H. E. Fischer, *Inorganic Chemistry*, 2011, **50**, 6146-6151.
9. L. Desgranges, G. Baldinozzi, G. Rousseau, J.-C. Nièpce and G. Calvarin, *Inorganic Chemistry*, 2009, **48**, 7585-7592.
10. S. Karcher, R. Mohun, T. Olds, M. Weber, K. Kriegsman, X. Zhao, X. Guo, C. Corkhill, D. Field and J. McCloy, *Journal of Raman Spectroscopy*, 2022, **n/a**.
11. F. Garrido, R. Ibberson, L. J. Nowicki and B. T. M. Willis, *Journal of Nuclear Materials*, 2003, **322**, 87-89.
12. G. Leinders, R. Bes, K. O. Kvashnina and M. Verwerft, *Inorganic Chemistry*, 2020, DOI: 10.1021/acs.inorgchem.9b03702.
13. G. Leinders, R. Delville, J. Pakarinen, T. Cardinaels, K. Binnemans and M. Verwerft, *Inorganic Chemistry*, 2016, **55**, 9923-9936.
14. L. Nowicki, F. Garrido, A. Turos and L. Thomé, *Journal of Physics and Chemistry of Solids*, 2000, **61**, 1789-1804.
15. G. C. Allen and P. A. Tempest, *Journal of The Chemical Society-dalton Transactions*, 1982, 2169-2173.
16. S. Aronson, R. Roof and J. Belle, *The Journal of Chemical Physics*, 1957, **27**, 137-144.
17. P. Taylor, *Journal of Nuclear Materials*, 2005, **344**, 206-212.
18. J. M. Elorrieta, L. J. Bonales, N. Rodríguez-Villagra, V. G. Baonza and J. Cobos, *Physical Chemistry Chemical Physics*, 2016, **18**, 28209-28216.
19. J. M. Elorrieta, L. J. Bonales, N. Rodríguez-Villagra, V. G. Baonza and J. Cobos, *MRS Advances*, 2017, **2**, 675-680.
20. D. Manara and B. Renker, *Journal of Nuclear Materials*, 2003, **321**, 233-237.
21. D. H. M. Lin, D. Manara, Z. Varga, A. Berlizov, T. Fanghanel and K. Mayer, *Radiochimica Acta*, 2013, **101**, 779.
22. M. Naji, N. Magnani, L. J. Bonales, S. Mastromarino, J. Y. Colle, J. Cobos and D. Manara, *Physical Review B*, 2017, **95**, 104307.
23. D. Manara, M. Naji, S. Mastromarino, J. M. Elorrieta, N. Magnani, L. Martel and J. Y. Colle, *Journal of Nuclear Materials*, 2018, **499**, 268-271.
24. P. G. Marlow, J. P. Russell and J. R. Hardy, *The Philosophical Magazine: A Journal of Theoretical Experimental and Applied Physics*, 1966, **14**, 409-410.
25. S. H. Rondahl, F. Pointurier, L. Ahlinder, H. Ramebäck, O. Marie, B. Ravat, F. Delaunay, E. Young, N. Blagojevic, J. R. Hester, G. Thorogood, A. N. Nelwamondo, T. P. Ntsoane, S. K. Roberts and K. S. Holliday, *Journal of radioanalytical and nuclear chemistry*, 2018, **315**, 395-408.
26. M. Amme, B. Renker, B. Schmid, M. P. Feth, H. Bertagnolli and W. Dobelin, *Journal of Nuclear Materials*, 2002, **306**, 202-212.

27. T. Livneh and E. Sterer, *Physical Review B*, 2006, **73**, 085118.

28. L. Desgranges, G. Baldinozzi, P. Simon, G. Guimbretiere and A. Canizares, *Journal of Raman Spectroscopy*, 2011, **43**, 455-458.

29. H. He and D. Shoesmith, *Physical chemistry chemical physics : PCCP*, 2010, **12**, 8108-8117.

30. C. Jegou, M. Gennisson, S. Peuget, L. Desgranges, G. Guimbretière, M. Magnin, Z. Talip and P. Simon, *Journal of Nuclear Materials*, 2015, **458**, 343-349.

31. T. Livneh, *Physical Review B*, 2022, **105**, 045115.

32. M. Razdan, M. Trummer, D. Zagidulin, M. Jonsson and D. W. Shoesmith, *Electrochimica Acta*, 2014, **130**, 29-39.

33. I. S. Butler, G. C. Allen and N. A. Tuan, *Applied Spectroscopy*, 1988, **42**, 901-902.

34. M. L. Palacios and S. H. Taylor, *Applied Spectroscopy*, 2000, **54**, 1372-1378.

35. D. Ho Mer Lin, D. Manara, P. Lindqvist-Reis, T. Fanghänel and K. Mayer, *Vibrational Spectroscopy*, 2014, **73**, 102-110.

36. A. Miskowiec, J. L. Niedziela, T. L. Spano, M. W. Ambrogio, S. Finkeldei, R. Hunt and A. E. Shields, *Journal of Nuclear Materials*, 2019, **527**, 151790.

37. M. J. Lipp, Z. Jenei, J. Park-Klepeis and W. J. Evans, *Raman Investigation of The Uranium Compounds  $U_3O_8$ ,  $UF_4$ ,  $UH_3$  and  $UO_3$  under Pressure at Room Temperature*, Lawrence Livermore National Lab. (LLNL), Livermore, CA (United States), 2011.

38. R. Driscoll, University of Bath, 2016.

39. P. Kegler, F. Pointurier, J. Rothe, K. Dardenne, T. Vitova, A. Beck, S. Hammerich, S. Potts, A.-L. Faure, M. Klinkenberg, F. Kreft, I. Niemeyer, D. Bosbach and S. Neumeier, *MRS Advances*, 2021, **6**, 125-130.

40. G. Guimbretière, L. Desgranges, A. Canizarès, G. Carlot, R. Caraballo, C. Jégou, F. Duval, N. Rimboux, M. R. Ammar and P. Simon, *Applied Physics Letters*, 2012, **100**, 251914.

41. A. Milena-Pérez, L. J. Bonales, N. Rodríguez-Villagra, S. Fernández, V. G. Baonza and J. Cobos, *Journal of Nuclear Materials*, 2021, **543**, 152581.

42. C. Jégou, R. Caraballo, S. Peuget, D. Roudil, L. Desgranges and M. Magnin, *Journal of Nuclear Materials*, 2010, **405**, 235-243.

43. G. Rousseau, L. Desgranges, F. Charlot, N. Millot, J. C. Nièpce, M. Pijolat, F. Valdivieso, G. Baldinozzi and J. F. Bérar, *Journal of Nuclear Materials*, 2006, **355**, 10-20.

44. G. C. Allen, I. S. Butler and T. Nguyen Anh, *Journal of Nuclear Materials*, 1987, **144**, 17-19.

45. J. M. Elorrieta, L. J. Bonales, M. Naji, D. Manara, V. G. Baonza and J. Cobos, *Journal of Raman Spectroscopy*, 2018, **49**, 878-884.

46. V. Petříček, M. Dušek and L. Palatinus, *Zeitschrift für Kristallographie - Crystalline Materials*, 2014, **229**, 345-352.

47. T. A. Olds, S. E. Karcher, K. W. Kriegsman, X. Guo and J. S. McCloy, *Journal of Nuclear Materials*, 2020, **530**, 151959.

48. J. S. Anderson, L. E. J. Roberts and E. A. Harper, *Journal of the Chemical Society (Resumed)*, 1955, DOI: 10.1039/JR9550003946, 3946-3959.

49. H. M. Rietveld, *Journal of Applied Crystallography*, 1969, **2**, 65-71.

50. G. Leinders, T. Cardinaels, K. Binnemans and M. Verwerft, *Journal of Nuclear Materials*, 2015, **459**, 135-142.

51. G. Leinders, G. Baldinozzi, C. Ritter, R. Saniz, I. Arts, D. Lamoen and M. Verwerft, *Inorganic Chemistry*, 2021, **60**, 10550-10564.

52. G. C. Allen, P. A. Tempest and J. W. Tyler, *Journal of the Chemical Society, Faraday Transactions 1: Physical Chemistry in Condensed Phases*, 1988, **84**, 4061-4072.

53. P. A. Tempest, P. M. Tucker and J. W. Tyler, *Journal of Nuclear Materials*, 1988, **151**, 269-274.

54. G. Leinders, J. Pakarinen, R. Delville, T. Cardinaels, K. Binnemans and M. Verwerft, *Inorganic Chemistry*, 2016, **55**, 3915-3927.

55. G. Talsky, *Derivative spectrophotometry: low and high order*, VCH Publishers, 1994.

56. L. J. Bonales, J. M. Elorrieta, A. Lobato and J. Cobos, in *Applications of Molecular Spectroscopy to Current Research in the Chemical and Biological Sciences*, ed. D. M. Stauffer, INTECH open science, 2016, vol. 1.

57. J. Cobos, D. Papaioannou, J. Spino and M. Coquerelle, *Journal of Alloys and Compounds*, 1998, **271-273**, 610-615.

58. B. Hanson, *The burnup dependence of light water reactor spent fuel oxidation*, Pacific Northwest National Laboratory, Richland, Washington 99352, 1998.

59. J.-W. Choi, R. J. McEachern, P. Taylor and D. D. Wood, *Journal of Nuclear Materials*, 1996, **230**, 250-258.

60. J. M. Elorrieta, D. Manara, L. J. Bonales, J. F. Vigier, O. Dieste, M. Naji, R. C. Belin, V. G. Baonza, R. J. M. Konings and J. Cobos, *Journal of Nuclear Materials*, 2017, **495**, 484-491.

61. L. Quémard, L. Desgranges, V. Bouineau, M. Pijolat, G. Baldinozzi, N. Millot, J.-C. Nièpce and A. Poulesquen, *Journal of the European Ceramic Society*, 2009, **29**.

62. L. Desgranges, H. Palancher, M. Gamaléri, J. S. Micha, V. Optasanu, L. Raceanu, T. Montesin and N. Creton, *Journal of Nuclear Materials*, 2010, **402**, 167-172.

63. J. Schoenes, *Physics Reports*, 1980, **63**, 301-336.

64. J. D. Axe and G. D. Pettit, *Physical Review*, 1966, **151**, 676-680.